

Super-Resolution Second-Harmonic Generation Imaging with Multifocal Structured Illumination Microscopy

Chenshuang Zhang, Fangrui Lin, Yong Zhang, Haozhi Yang, Danying Lin, Jun He, Changrui Liao, Xiaoyu Weng, Liwei Liu, Yiping Wang, Bin Yu,* and Junle Qu*



Cite This: *Nano Lett.* 2023, 23, 7975–7982



Read Online

ACCESS |

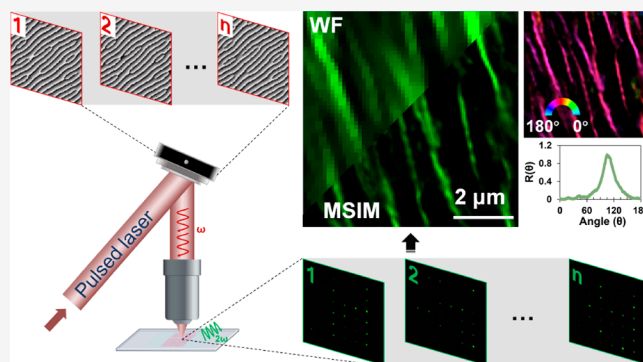
Metrics & More

Article Recommendations

Supporting Information

ABSTRACT: Second-harmonic generation (SHG) is a non-invasive imaging technique that enables the exploration of physiological structures without the use of an exogenous label. However, traditional SHG imaging is limited by optical diffraction, which restricts the spatial resolution. To break this limitation, we developed a novel approach called multifocal structured illumination microscopy-SHG (MSIM-SHG). By combination of SHG with MSIM, SHG-based super-resolution imaging of material molecules can be achieved, and this SHG super-resolution imaging has a wide range of applications for biological tissues and cells. MSIM-SHG achieved a lateral full width at half-maximum (fwhm) of 147 ± 13 nm and an axial fwhm of 493 ± 47 nm by imaging zinc oxide (ZnO) particles. Furthermore, MSIM-SHG was utilized to quantify collagen fiber alignment in various tissues such as the ovary, muscle, heart, kidney, and cartilage, demonstrating its feasibility for identifying collagen characteristics. MSIM-SHG has potential as a powerful tool for clinical diagnosis and biological research.

KEYWORDS: second-harmonic generation, super-resolution imaging, multifocal structured illumination microscopy



muscle, heart, kidney, and cartilage, demonstrating its feasibility for identifying collagen characteristics. MSIM-SHG has potential as a powerful tool for clinical diagnosis and biological research.

Second-harmonic generation (SHG) is a nonlinear-optical process in which two photons interact with a nonlinear material and instantaneously convert their energy into a new single photon with half the wavelength of the original photons.¹ SHG imaging is an emerging technology for biological imaging that possesses an intrinsic optical sectioning capability and eliminates the need for exogenous labels.² SHG mainly occurs in fibrillar collagen because it has a highly ordered, noncentrosymmetric structure. Fibrillar collagen is the predominant protein in the human body, being the principal component of connective tissues.^{3,4} Pathological changes in collagen fiber networks in terms of fiber alignment and waviness have also been observed in cancers, fibrosis, and inflammations.^{5–8} Many studies have shown that SHG microscopy can be used for disease diagnosis by imaging the concentration and distribution of collagen.⁸ However, the diffraction-limited resolution of SHG microscopy restricts further exploration of the relationship between collagen in disease formation and progression.

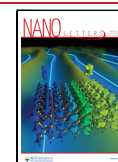
Enhancing SHG using plasmonic nanostructures and nanoantennas has gained much attention, while plasmon-enhanced SHG has been primarily applied for the measurement of bulk properties of the materials/molecules.^{9,10} Sahu et al. achieved visualization and orientation imaging of individual molecules in the presence of plasmonic silver nanohole arrays, but there is still much work to be done from nanophotonics to

the applications of super-resolution SHG imaging in biological cells and tissues.¹¹ Super-resolution techniques such as stimulated emission depletion (STED), stochastic optical reconstruction microscopy (STORM), and structured illumination microscopy (SIM) have been developed to exceed the conventional diffraction limit in fluorescence microscopy.^{12–14} However, the development of super-resolution techniques for SHG imaging is rare. Johnson et al. employed dielectric spheres placed on a sample's surface to focus light into the photonic nanojet (PNJ) phenomena for achieving SHG imaging beyond the diffraction limit,¹⁵ but optimal resolution and field of view were realized only at a specific Z-axis position. Based on image scanning microscopy, Gregor et al. achieved super-resolved SHG images through digital image processing on excessively large image recordings by single-focus scanning.¹⁶ However, this approach has limitations in terms of the total acquisition time. Recently, Stanciu et al. introduced rescanned SHG microscopy, which utilizes optical photon reassignment instead of digital processing.¹⁷ This method

Received: May 22, 2023

Revised: August 25, 2023

Published: August 29, 2023



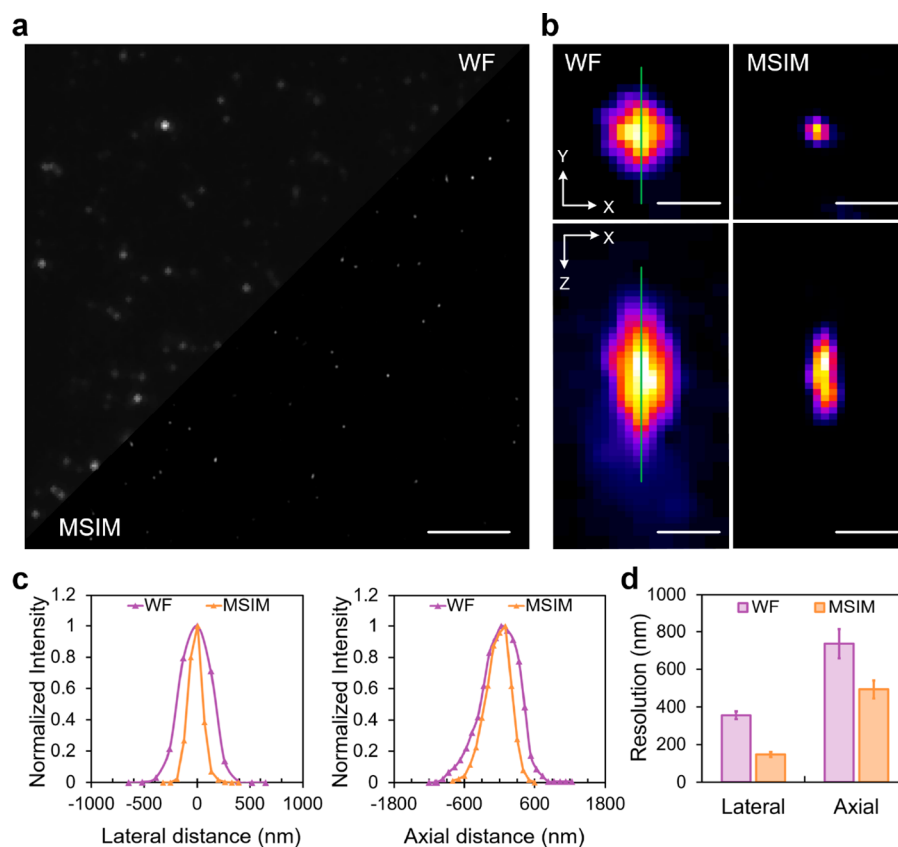


Figure 1. Estimated resolution of the MSIM-SHG system. (a) SHG images of ZnO particles on a coverslip surface with wide-field resolution and super-resolution, respectively. Scale bars: 5 μm . (b) ZnO images viewed in lateral (top) and axial (bottom) cuts through the image stacks. From left to right: SHG image with wide-field resolution and super-resolution. Scale bars: 0.5 μm . (c) Comparative line profiles through the center of each lateral (left) and axial (right) bead image further emphasizing improvement after MSIM reconstruction. (d) Statistical comparison of the estimated lateral (left) and axial (right) resolution derived from 26 particles. Means and standard deviations are shown.

overcomes the limitations of single-focus scanning but introduces the problem of nonlinear signals mixing with instrument noise.

Multiple groups have presented the use of Fourier transform (FT) to characterize the morphological properties of collagen fibers.^{18,19} In general, the information in this spatial frequency image can be compressed into a line plot of the spatial frequency intensity as a function of the angle, which quantitatively assesses the orientation of collagen fibers. Furthermore, this has been implemented in several ways, such as by thresholding and fitting the spatial frequency image to an ellipse²⁰ for describing the directional anisotropy or to a line for determining the preferred orientation.²¹ Image thresholding is prone to bias and may output a biased resulting analysis. In a slow-fitting operation, a reliable known function is required. To measure the local organization of the collagen fibers, some groups access the Hough transform of small tiles of the image and compute the entropy distribution, which represents the probability of finding the direction of fibers along a dominant direction.¹⁸ However, binary operation still causes some structural information loss. Additionally, there is a group that has explored the use of texture analysis based on first-order statistics and second-order statistics such as gray-level co-occurrence matrix to extract SHG image features,²² but high computational complexity limits its practical application. Interestingly, a morphological opening is applied using a rotated structuring element (Strel) to extract fibrils in the Strel direction.¹⁹ It is worth noting that the length of the

segment has an important influence on the determination of the local orientation. Computing large matrices of different image features based on computational machine learning methods, despite their powerful capabilities,²³ remains a challenge in avoiding overfitting and merging to promote generalization of learning algorithms.

Herein, we introduce a method called multifocal structured illumination second-harmonic generation microscopy (MSIM-SHG) for super-resolution SHG imaging with a high signal-to-noise ratio. MSIM-SHG records the nonlinear signal generated by the sample (during the excitation dwell time) as well as the noise of the instrument (during the nondwell time) individually in separate images, which provides an opportunity for easy postprocessing noise deduction. Furthermore, we present a quickly unbiased algorithm based on the Fourier transform and Radon transform, which does not require fitting or thresholding. The efficient algorithm, called fiber alignment anisotropy, characterizes the symmetry of SHG images ranging from 0 (randomized fibers) to 1 (perfect alignment). MSIM-SHG was used to quantify collagen fiber alignment in ovary, muscle, heart, kidney, and cartilage tissues, demonstrating its feasibility for identifying collagen characteristics. SHG imaging with diffraction-limited resolution distinguishes only the collagen content and overall characteristics in tissues. Significantly, MSIM-SHG can clearly observe the distribution angle of a single collagen, allowing for the observation of various characteristics of collagen in various kinds of tissues. This significant super-resolution SHG microscopy will provide

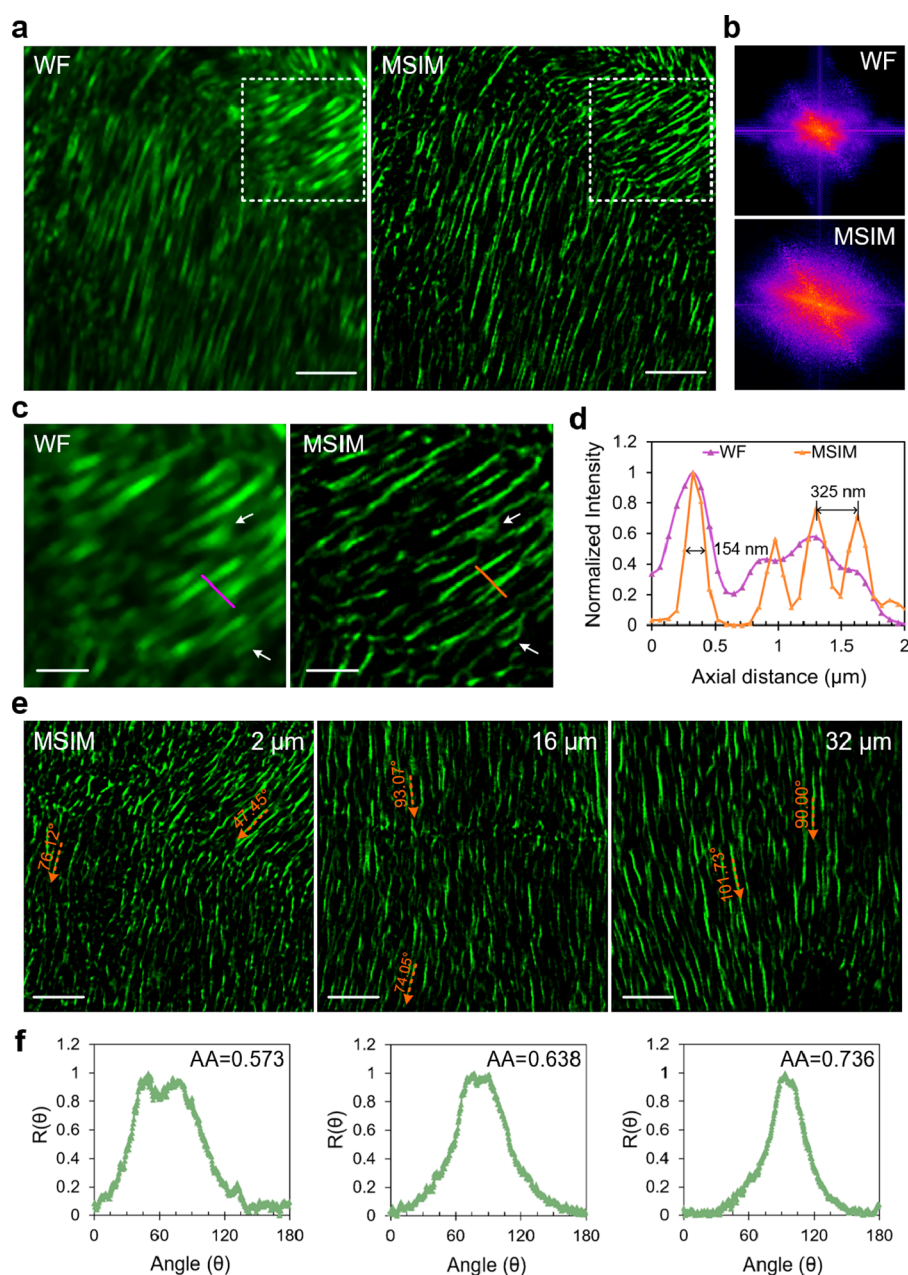


Figure 2. SHG images of a mouse tail tendon with MSIM-SHG. (a) Comparison of SHG images with wide-field resolution and super-resolution. Scale bars: 5 μm . (b) Lateral resolution improvement after MSIM reconstruction is quantified in the spatial frequency images (WF, top; MSIM, bottom). (c) Higher magnification views of the dashed square region in (a). Scale bars: 2 μm . (d) Intensity characterization of the resolution enhancement corresponding to (c). (e) SHG images with super-resolution at various depths. Scale bars: 5 μm . (f) Angular content distributions and values of fiber alignment anisotropy corresponding to (e).

an advanced and powerful tool for nanophotonics, biological research, and pathological diagnosis.

The performance of MSIM-SHG was assessed by imaging 90 nm zinc oxide (ZnO) particles on a coverslip surface (Figure 1). Figure 1a shows a significant improvement in resolution achieved by MSIM-SHG. Additionally, exemplary images of ZnO with wide-field resolution and super-resolution are presented in lateral (top) and axial (bottom) cuts through the image stacks, as shown in Figure 1b, along with their corresponding intensity profiles in Figure 1c. In the WF-SHG image, the lateral full width at half-maximum (fwhm) is 346 nm, and the axial fwhm is 730 nm. After MSIM reconstruction, the lateral fwhm improved to 148 nm and the axial fwhm was

reduced to 483 nm. Moreover, Figure 1d shows the statistical lateral and axial resolution values from 26 ZnO particles (lateral fwhm 356 ± 21 nm, axial fwhm 736 ± 77 nm) with wide-field resolution. After MSIM reconstruction, we obtained a lateral fwhm of 147 ± 13 nm and an axial fwhm of 493 ± 47 nm.

To demonstrate the resolution improvement in biological imaging, we utilized a mouse tail tendon sample without staining. Figure 2a shows the SHG images of the mouse tendon with wide-field resolution and with super-resolution. Figure 2b shows the spatial frequency space images used to estimate the improvement of spatial resolution corresponding to Figure 2a. Figure 2c shows the enlarged square regions in

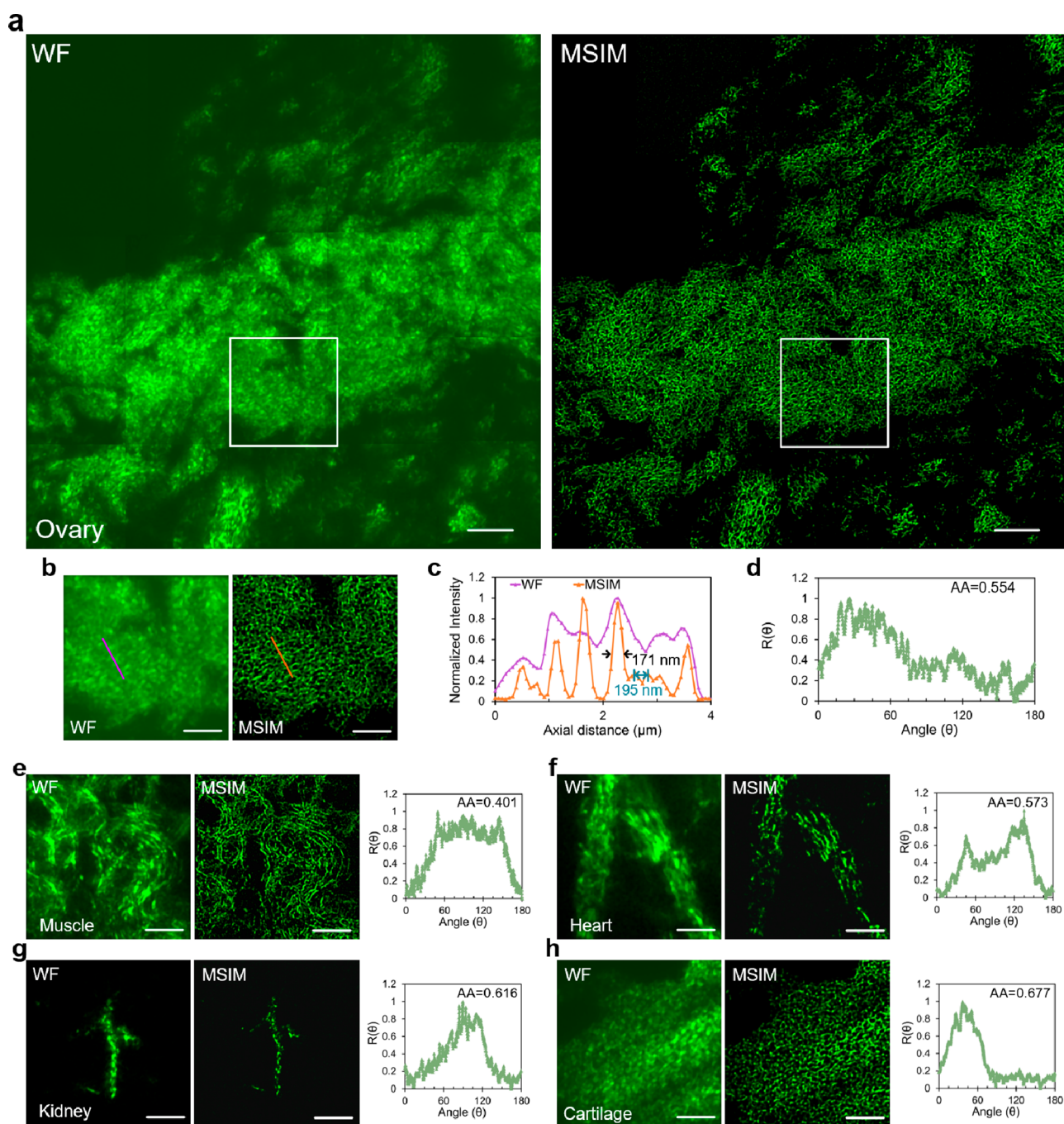


Figure 3. SHG images with super-resolution and the quantifications of collagen fiber alignment acquired from various types of biological tissues. (a) Comparison of collagen fibers from the ovary with wide-field resolution and super-resolution. Scale bars: 10 μm . (b) Higher magnification views of the square region in (a). Scale bars: 5 μm . (c) Intensity characterizations of the resolution enhancement corresponding to (b). (d) Angular content distribution and the value of fiber alignment anisotropy corresponding to (b). (e–h) Comparisons of SHG images of collagen fibers with wide-field resolution and super-resolution, the angular content distributions, and fiber alignment anisotropy values from leg muscle, heart, kidney, and cartilage, respectively. Scale bars: 5 μm .

Figure 2a, and Figure 2d shows the normalized intensity profiles for Figure 2c. After applying MSIM, there is an apparent improvement in the contrast of the MSIM image (154 nm) compared to that of the WF image, resolving adjacent collagen fibers with a distance of 325 nm. Using the information in spatial frequency space images, the orientation of every collagen fibril in the image was color mapped as shown in Figure S3. To further demonstrate the feasibility of MSIM-SHG, we imaged the mouse tail tendon at different depths. The WF and MSIM images of different imaging depths

($z = 2, 16, \text{ and } 32 \mu\text{m}$) are shown in Figure 2e. The fiber angles in the image were determined using the angle tool from the ImageJ toolbar by manual operation (orange dashed arrow and angle values). However, manual analysis is undoubtedly time-consuming. To quickly extract collagen fiber alignment for disease diagnostics, SHG images $I(x,y)$ were computed by 2D FT, obtaining $I(u,v)$. Then, we used the Radon function to compute projections of the images along directions θ from 0° to 180° (along the path passing the center of $I(u,v)$)

$$R(\theta)(x') = \int f(x' \cos \theta - y' \sin \theta, x' \sin \theta + y' \cos \theta) dy' \quad (1)$$

where $x' = 0$ and $R(\theta)$ represents the angular content distribution (Figure 2f). Furthermore, to describe the fiber alignment anisotropy, we present alignment anisotropy (AA) (ranging from 0 (randomized fibers) to 1 (perfect alignment)) to characterize the order of the fibers as follows:

$$AA = 1 - \frac{\int R(\theta) d\theta}{\int \max(R(\theta)) d\theta} \quad (2)$$

To evaluate the algorithm, a series of simulated structures is generated, as shown in Figure S4, which gives the simulated distribution of collagen fibers from high to random alignment. The corresponding color maps of the local orientation, angular distributions, and values of fiber alignment anisotropy show results highly consistent with the expected values.

The typical fiber size of fibrillar collagen is 40–200 nm, which is below the diffraction limit of conventional SHG.²⁴ Here, we used formalin-fixed samples of various unstained mouse tissues to demonstrate the capacity of the MSIM-SHG technique on thinly sliced (5 μm) specimens (Figure 3). A WF image and corresponding super-resolution image of the ovary are shown in Figure 3a. Compared with high-magnification SHG imaging with wide-field resolution (Figure 3b), the MSIM image exhibited a significant improvement in resolution and signal-to-noise ratio, enabling visualization of collagen fibers (171 nm). The image intensity profiles of the fibrillar collagen structures (Figure 3c) show that fibers can be much more clearly distinguished when they are observed using MSIM-SHG, resolving adjacent collagen fibers with a distance of 195 nm. The angular distribution and computed fiber alignment anisotropy are shown in Figure 3d. The images from leg muscles, heart, kidneys, and cartilage were obtained using the same protocols (Figure 3e–h). The content and distribution of collagen fibers in these tissues are highly characteristic. In collagen fibers in muscle, some bundles of fibers intertwine to generate force and movement (Figure 3e). In the heart, fiber bundles often assume a weavlike structure that provides a structural framework to the cardiac myocytes, imparting stiffness to the myocardial wall and aiding force transmission (Figure 3f). The capillary basement membrane in kidneys is important for providing physical and biochemical cues to the overlying cells, sculpting the tissue into its correct size and shape (Figure 3g). As shown in Figure 3h, the cartilage has collagen fibrils and lacunae (spaces within the tight organization of collagen fibrils that contain chondrocytes cells). Furthermore, we also have imaged the cartilage with a larger field of view and in Z-axis scanning (Figure S5), which further demonstrates the dense organization of collagen fibrils in cartilage, and two typical patterns (disordered and parallel) of collagen organization can be identified from the 3D imaging of collagen.

Overall, the MSIM-SHG system provides a significant improvement in the resolution of SHG imaging, visualizing biological molecules such as collagen fibrils that are smaller than the diffraction limit. The algorithm produces a single-parameter output of the alignment, making it easy to use in clinical applications of SHG imaging technology. Compared to several approaches for SHG imaging beyond the diffraction limit, MSIM-SHG does not require special processing on

samples (e.g., placing dielectric spheres on the sample's surface for PNJ), and the imaging depth can be easily selected by moving the sample position (or the height of objective). Furthermore, the MSIM-SHG technique captures a series of raw images instead of a single super-resolution image obtained with rescanned SHG microscopy. As a result, by applying postprocessing techniques, a super-resolution SHG image with a higher signal-to-noise ratio can be obtained. The technique involves extracting only the nonlinear focus and performing pixel reassignment to surpass the diffraction limit while simultaneously eliminating instrument noise. In MSIM-SHG, multiple excitation foci are generated within a single frame to enhance imaging speed compared to that of single-focus scanning. As long as the foci are adequately sparse, crosstalk resulting from parallel excitation is negligible.

The precise design of excitation patterns (multifocal array) is crucial for avoiding artifacts and ensuring uniform scanning of samples throughout the entire field of view. The accurate positions of the excitation patterns are critical in MSIM for applying digital pinholes and image reconstruction. These factors are particularly significant when imaging highly scattering or deep tissues, where aberrations and noise can cause artifacts in the final super-resolution image. We computationally determine the excitation pattern in every raw image to identify the exact excitation.^{25,26} Additionally, combining MSIM with nonlinear imaging techniques such as two-photon excitation or SHG can reduce the effects of sample scattering and minimize artifacts in MSIM.^{16,27}

Polarization-resolved SHG allows for the quantification of collagen fibril orientation,^{28,29} even three-dimensional orientation.³⁰ However, these polarization analyses are mostly based on traditional SHG microscopy with limited resolution, which to some extent impairs the accuracy of quantitative collagen orientation (the average orientation of adjacent collagen fibrils rather than the exact orientation of a single collagen fibril).²⁸ MSIM-SHG resolves the local distribution of fibrils in the XY plane, mainly breaking the limited spatial resolution of traditional SHG microscopy to distinguish collagen fibrils with distances below the optical diffraction limit. Additionally, our algorithm not only provides global information about orientation in the field of view but also enables the extraction of the orientation in every collagen fibril. It is difficult to obtain the orientation of a separate pixel without combining polarization. Fortunately, combining MSIM-SHG and polarization is completely feasible. For example, in the MSIM-SHG system, the laser linear polarization state is rotated from 0° to 180°, and raw images are captured every 20°. Polarization parameters can be determined by performing nonlinear data fitting. However, there are still some issues that need to be overcome when MSIM-SHG is combined with polarization. For example, a large number of raw images under each polarization excitation is required, which is time-consuming and sensitive to system drift and environmental vibration. In the future, if the polarization direction of each pixel can be well extracted from the super-resolution SHG image, it will promote analysis of the collagen ultrastructure and further improve the sensitivity of pathological diagnosis.

Experimental Setup. As shown in Figure S1, the MSIM-SHG system mainly comprised two light paths for near-infrared illumination (red) and visible detection (green). The intensity of the 1036 nm femtosecond laser from the laser source (YSL, Femto YLTM) was controlled by a $1/2 \lambda$ wave plate (Thorlabs, AHWP05M-980) and a polarizing beam

splitter (PBS) cube (Thorlabs, CCM1-PBS252). Then, the laser beam was expanded by a pair of NIR achromatic lenses (L1 and L2) before being reflected to an NIR-responsive high-speed phase-only spatial light modulator (SLM NIR, Meadowlark, HSP1920-1152) at $\sim 10^\circ$. Another $1/2 \lambda$ wave plate was placed in front of the SLM to facilitate the suitable polarization alignment of the SLM. Another pair of NIR achromatic relay lenses (L3 and L4) were used to create a magnified image of the SLM at the rear pupil plane of the imaging objective (Nikon, CFI Apo LWD 25XW, 1.1 NA, and 2 mm WD). The SLM loaded the phase patterns to generate and shift a diffraction-limited multifocal array for nonlinear illumination at the sample plane. An iris (Thorlabs, ID25) was placed in the focal plane of L3 (conjugate with the sample plane) to filter unnecessary diffraction orders generated by the SLM. Two filters, SP850 (Thorlabs, FESH0850) and BP520/15 (Semrock, FF01-520/15-25), were placed after L5 to isolate the SHG signal before being collected on the EMCCD (Andor, Life 888, 1024 pixels \times 1024 pixels; $13 \mu\text{m} \times 13 \mu\text{m}$). It is worth noting that the aforementioned SLM conjugates with the rear pupil plane of the objective. The sample plane is magnified 100-fold and conjugated with the EMCCD (the effective pixel size is 130 nm).

To generate a multifocal array at the sample plane by the SLM ($\sim 50\%$ laser power is retained at the rear pupil plane of the objective), the weighted Gerchberg–Saxton (WGS)³¹ algorithm was adopted to determine the programmable phase patterns loaded onto the SLM. Furthermore, the shift of the multifocal array was realized by adding a corresponding linear grating phase to the previous pattern. By changing the linear grating phase pattern sequentially, focal array scanning could be realized to cover the full imaging field.

Data Acquisition. For SHG imaging, the illumination power of a single focus at the samples was approximately 9 mW. The illumination patterns with 6×6 foci in $4.74 \mu\text{m}$ spacing were used to scan the sample, and 1296 raw images were recorded for each field of view ($\sim 28 \times 28 \mu\text{m}$). The electron multiplication gain of the EMCCD was set to 180 nm for all measurements. The SLM and EMCCD are synchronized at 40 Hz.

Data Processing for Wide-Field and MSIM-SHG Image. In the MSIM-SHG system, an SLM is triggered to load phase patterns (Figure S2a) in synchronization with EMCCD frames. During the MSIM scanning process, multifocal arrays traverse the entire field of view pixel by pixel, and the corresponding signal is recorded in a series of raw images (Figure S2b). For each pixel of the images, the nonlinear signal of the sample is recorded in one of the images when the laser focus dwells on the corresponding position (dwell time), while instrument noise is recorded in other images when the laser illuminates noncorresponding positions (non-dwell time). As shown in Figure S2c, a WF image is obtained by summing the raw images directly. Furthermore, SHG raw images are postprocessed to improve the signal-to-noise ratio and resolution. After filtering and pinholing, only the nonlinear focus is extracted for the next pixel reassignment to improve resolution, while the instrument noise is discarded, improving the resulting intermediate images' signal-to-noise ratio. Finally, a super-resolution SHG image is obtained by summing up the intermediate images and further deconvolution. Eliminating instrument noise improves the signal-to-noise ratio of the resulting images. Pixel reassignment and further deconvolution are key steps to improving resolution.¹⁶ The

detailed theory of MSIM-SHG is described in the Supporting Information.

Sample Preparation. The various biological tissues were collected from 3 month old C57BL/6 mice. The tail tendons were washed with phosphate-buffered saline and then mounted on a microscope slide immediately for MSIM-SHG imaging in the Z-direction (Figure 2). The other tissues (ovary, muscle, heart, kidney, and cartilage in Figure 3) were fixed in 4% paraformaldehyde for 12 h and infiltrated with paraffin for long-term preservation. Thin slices of $5 \mu\text{m}$ were taken using a microtome (Leica, RM2016), followed by dewaxing with xylene and graded alcohols according to a conventional protocol. None of the samples were stained.

■ ASSOCIATED CONTENT

SI Supporting Information

The Supporting Information is available free of charge at <https://pubs.acs.org/doi/10.1021/acs.nanolett.3c01903>.

MSIM-SHG system, data acquisition and processing, local orientation of biological tissues and simulated fibers, and theory of MSIM-SHG (PDF)

■ AUTHOR INFORMATION

Corresponding Authors

Bin Yu – Key Laboratory of Optoelectronic Devices and Systems of Ministry of Education and Guangdong Province, College of Physics and Optoelectronic Engineering, Shenzhen University, Shenzhen 518060, People's Republic of China; orcid.org/0000-0002-8698-0155; Email: yubin@szu.edu.cn

Junle Qu – Key Laboratory of Optoelectronic Devices and Systems of Ministry of Education and Guangdong Province, College of Physics and Optoelectronic Engineering, Shenzhen University, Shenzhen 518060, People's Republic of China; orcid.org/0000-0001-7833-4711; Email: jlqu@szu.edu.cn

Authors

Chenshuang Zhang – Key Laboratory of Optoelectronic Devices and Systems of Ministry of Education and Guangdong Province, College of Physics and Optoelectronic Engineering, Shenzhen University, Shenzhen 518060, People's Republic of China; orcid.org/0000-0002-6655-9494

Fangrui Lin – Key Laboratory of Optoelectronic Devices and Systems of Ministry of Education and Guangdong Province, College of Physics and Optoelectronic Engineering, Shenzhen University, Shenzhen 518060, People's Republic of China

Yong Zhang – Key Laboratory of Optoelectronic Devices and Systems of Ministry of Education and Guangdong Province, College of Physics and Optoelectronic Engineering, Shenzhen University, Shenzhen 518060, People's Republic of China

Haozhi Yang – Key Laboratory of Optoelectronic Devices and Systems of Ministry of Education and Guangdong Province, College of Physics and Optoelectronic Engineering, Shenzhen University, Shenzhen 518060, People's Republic of China

Danying Lin – Key Laboratory of Optoelectronic Devices and Systems of Ministry of Education and Guangdong Province, College of Physics and Optoelectronic Engineering, Shenzhen University, Shenzhen 518060, People's Republic of China; orcid.org/0000-0002-9121-1916

Jun He – Key Laboratory of Optoelectronic Devices and Systems of Ministry of Education and Guangdong Province, College of Physics and Optoelectronic Engineering, Shenzhen University, Shenzhen 518060, People's Republic of China; orcid.org/0000-0002-9417-2019

Changrui Liao – Key Laboratory of Optoelectronic Devices and Systems of Ministry of Education and Guangdong Province, College of Physics and Optoelectronic Engineering, Shenzhen University, Shenzhen 518060, People's Republic of China; orcid.org/0000-0003-3669-5054

Xiaoyu Weng – Key Laboratory of Optoelectronic Devices and Systems of Ministry of Education and Guangdong Province, College of Physics and Optoelectronic Engineering, Shenzhen University, Shenzhen 518060, People's Republic of China

Liwei Liu – Key Laboratory of Optoelectronic Devices and Systems of Ministry of Education and Guangdong Province, College of Physics and Optoelectronic Engineering, Shenzhen University, Shenzhen 518060, People's Republic of China; orcid.org/0000-0002-4593-665X

Yiping Wang – Key Laboratory of Optoelectronic Devices and Systems of Ministry of Education and Guangdong Province, College of Physics and Optoelectronic Engineering, Shenzhen University, Shenzhen 518060, People's Republic of China

Complete contact information is available at:

<https://pubs.acs.org/10.1021/acs.nanolett.3c01903>

Notes

The authors declare no competing financial interest.

ACKNOWLEDGMENTS

The National Key R&D Program of China (2022YFF0712500), the National Natural Science Foundation of China (61975131, 62175166, 61835009, 62127819, 62235007, and 62275165), the Shenzhen Science and Technology Program (JCYJ20200109105411133 and JCYJ20220818100202005), and the Shenzhen Key Laboratory of Photonics and Biophotonics (ZDSYS20210623092006020) are acknowledged for support of this work.

REFERENCES

- (1) Franken, P. A.; Hill, A. E.; Peters, C. W.; Weinreich, G. Generation of optical harmonics. *Phys. Rev. Lett.* **1961**, *7* (4), 118–119.
- (2) Campagnola, P. J.; Loew, L. M. Second-harmonic imaging microscopy for visualizing biomolecular arrays in cells, tissues and organisms. *Nat. Biotechnol.* **2003**, *21* (11), 1356–1360.
- (3) Puetzer, J. L.; Ma, T.; Sallent, I.; Gelmi, A.; Stevens, M. M. Driving Hierarchical Collagen Fiber Formation for Functional Tendon, Ligament, and Meniscus Replacement. *Biomaterials* **2021**, *269*, 120527.
- (4) Shoulders, M. D.; Raines, R. T. Collagen structure and stability. *Annu. Rev. Biochem.* **2009**, *78*, 929–958.
- (5) Neff, L. S.; Bradshaw, A. D. Cross your heart? Collagen cross-links in cardiac health and disease. *Cell Signal* **2021**, *79*, 109889.
- (6) Frangogiannis, N. G. The Extracellular Matrix in Ischemic and Nonischemic Heart Failure. *Circ. Res.* **2019**, *125* (1), 117–146.
- (7) Cisek, R.; Joseph, A.; Harvey, M.; Tokarz, D. J. F. i. P. Polarization-sensitive second harmonic generation microscopy for investigations of diseased collagenous tissues. *Front Phys.* **2021**, *9*, 726996.
- (8) Campagnola, P. J.; Dong, C. Y. Second harmonic generation microscopy: principles and applications to disease diagnosis. *Laser Photonics Rev.* **2011**, *5* (1), 13–26.

(9) Timpu, F.; Hendricks, N. R.; Petrov, M.; Ni, S.; Renaut, C.; Wolf, H.; Isa, L.; Kivshar, Y.; Grange, R. Enhanced Second-Harmonic Generation from Sequential Capillarity-Assisted Particle Assembly of Hybrid Nanodimers. *Nano Lett.* **2017**, *17* (9), 5381–5388.

(10) Shen, S.; Meng, L.; Zhang, Y.; Han, J.; Ma, Z.; Hu, S.; He, Y.; Li, J.; Ren, B.; Shih, T. M.; Wang, Z.; Yang, Z.; Tian, Z. Plasmon-Enhanced Second-Harmonic Generation Nanorulers with Ultrahigh Sensitivities. *Nano Lett.* **2015**, *15* (10), 6716–6721.

(11) Sahu, S. P.; Mahigir, A.; Chidester, B.; Veronis, G.; Gartia, M. R. Ultrasensitive Three-Dimensional Orientation Imaging of Single Molecules on Plasmonic Nanohole Arrays Using Second Harmonic Generation. *Nano Lett.* **2019**, *19* (9), 6192–6202.

(12) Rittweger, E.; Han, K. Y.; Irvine, S. E.; Egeling, C.; Hell, S. W. STED microscopy reveals crystal colour centres with nanometric resolution. *Nat. Photonics* **2009**, *3* (3), 144–147.

(13) Rust, M. J.; Bates, M.; Zhuang, X. Sub-diffraction-limit imaging by stochastic optical reconstruction microscopy (STORM). *Nat. Methods* **2006**, *3* (10), 793–795.

(14) Muller, C. B.; Enderlein, J. Image scanning microscopy. *Phys. Rev. Lett.* **2010**, *104* (19), 198101.

(15) Johnson, P. B.; Karvounis, A.; Singh, H. J.; Brereton, C. J.; Bourdakos, K. N.; Lunn, K.; Roberts, J. J. W.; Davies, D. E.; Muskens, O. L.; Jones, M. G.; Mahajan, S. Superresolved polarization-enhanced second-harmonic generation for direct imaging of nanoscale changes in collagen architecture. *Optica* **2021**, *8* (5), 674–685.

(16) Gregor, I.; Spiecker, M.; Petrovsky, R.; Grosshans, J.; Ros, R.; Enderlein, J. Rapid nonlinear image scanning microscopy. *Nat. Methods* **2017**, *14* (11), 1087–1089.

(17) Stanciu, S. G.; Hristu, R.; Stanciu, G. A.; Tranca, D. E.; Eftimie, L.; Dumitru, A.; Costache, M.; Stenmark, H. A.; Manders, H.; Cherian, A.; Tark-Dame, M.; Manders, E. M. M. Super-resolution re-scan second harmonic generation microscopy. *Proc. Natl. Acad. Sci. U. S. A.* **2022**, *119* (47), No. e2214662119.

(18) Bayan, C.; Levitt, M. J.; Miller, E.; Kaplan, D.; Georgakoudi, I. Fully automated, quantitative, noninvasive assessment of collagen fiber. *J. Appl. Phys.* **2009**, *105*, 102042.

(19) Bancelin, S.; Nazac, A.; Ibrahim, B. H.; Dokladal, P.; Decenciere, E.; Teig, B.; Haddad, H.; Fernandez, H.; Schanne-Klein, M. C.; De Martino, A. Determination of collagen fiber orientation in histological slides using Mueller microscopy and validation by second harmonic generation imaging. *Opt Express* **2014**, *22* (19), 22561.

(20) Ghazaryan, A.; Tsai, H. F.; Hayrapetyan, G.; Chen, W. L.; Chen, Y. F.; Jeong, M. Y.; Kim, C. S.; Chen, S. J.; Dong, C. Y. Analysis of collagen fiber domain organization by Fourier second harmonic generation microscopy. *J. Biomed Opt* **2013**, *18* (3), 031105.

(21) Rao, R. A. R.; Mehta, M. R.; Toussaint, K. C. Fourier transform-second-harmonic generation imaging of biological tissues. *Opt Express* **2009**, *17*, 14534.

(22) Mostaco-Guidolin, L. B.; Ko, A. C.; Wang, F.; Xiang, B.; Hewko, M.; Tian, G.; Major, A.; Shiomi, M.; Sowa, M. G. Collagen morphology and texture analysis: from statistics to classification. *Sci. Rep* **2013**, *3*, 2190–2199.

(23) Woessner, A. E.; Quinn, K. P. Improved segmentation of collagen second harmonic generation images with a deep learning convolutional neural network. *J. Biophotonics* **2022**, *15* (12), No. e202200191.

(24) Sherman, V. R.; Yang, W.; Meyers, M. A. The materials science of collagen. *J. Mech Behav Biomed Mater.* **2015**, *52*, 22–50.

(25) McGregor, J. E.; Mitchell, C. A.; Hartell, N. A. Post-processing strategies in image scanning microscopy. *Methods* **2015**, *88*, 28–36.

(26) Strohl, F.; Kaminski, C. F. A joint Richardson-Lucy deconvolution algorithm for the reconstruction of multifocal structured illumination microscopy data. *Methods Appl. Fluoresc* **2015**, *3* (1), 014002.

(27) Ingaramo, M.; York, A. G.; Wawrzusin, P.; Milberg, O.; Hong, A.; Weigert, R.; Shroff, H.; Patterson, G. H. Two-photon excitation improves multifocal structured illumination microscopy in thick

scattering tissue. *Proc. Natl. Acad. Sci. U. S. A.* **2014**, *111* (14), 5254–5259.

(28) Schmeltz, M.; Teulon, C.; Pinsard, M.; Hansen, U.; Alnawaiseh, M.; Ghoubay, D.; Borderie, V.; Mosser, G.; Aimé, C.; Légaré, F.; Latour, G.; Schanne-Klein, M. C. Circular dichroism second-harmonic generation microscopy probes the polarity distribution of collagen fibrils. *Optica* **2020**, *7* (11), 1469–1478.

(29) Harvey, M.; Cisek, R.; Alizadeh, M.; Barzda, V.; Kreplak, L.; Tokarz, D. High numerical aperture imaging allows chirality measurement in individual collagen fibrils using polarization second harmonic generation microscopy. *Nanophotonics* **2023**, *12* (11), 2061–2071.

(30) Reiser, K.; Stoller, P.; Knoesen, A. Three-Dimensional Geometry of Collagenous Tissues by Second Harmonic Polarimetry. *Sci. Rep* **2017**, *7* (1), 2642–2651.

(31) Kim, D.; Keesling, A.; Omran, A.; Levine, H.; Bernien, H.; Greiner, M.; Lukin, M. D.; Englund, D. R. Large-scale uniform optical focus array generation with a phase spatial light modulator. *Opt. Lett.* **2019**, *44* (12), 3178–3181.